Available online at www.sciencedirect.com
ScienceDirect
Journal of Power Sources 162 (2006) 1182–1191
JOURNAL OF POWER SOURCES
www.elsevier.com/locate/jpowsour

Numerical simulation of proton exchange membrane fuel cells at high operating temperature

Jie Peng, Seung Jae Lee *

Energy Lab, Samsung Advanced Institute of Technology, Mt. 14-1 Nongseo-Dong, Giheung-Gu, Yongin-Si, Gyeonggi-Do 446-712, South Korea

Received 23 June 2006; received in revised form 1 August 2006; accepted 1 August 2006
Available online 7 September 2006

Abstract

A three-dimensional, single-phase, non-isothermal numerical model for proton exchange membrane (PEM) fuel cell at high operating temperature ($T \geq 393$ K) was developed and implemented into a computational fluid dynamic (CFD) code. The model accounts for convective and diffusive transport and allows predicting the concentration of species. The heat generated from electrochemical reactions, entropic heat and ohmic heat arising from the electrolyte ionic resistance were considered. The heat transport model was coupled with the electrochemical and mass transport models. The product water was assumed to be vaporous and treated as ideal gas. Water transportation across the membrane was ignored because of its low water electro-osmosis drag force in the polymer polybenzimidazole (PBI) membrane. The results show that the thermal effects strongly affect the fuel cell performance. The current density increases with the increasing of operating temperature. In addition, numerical prediction reveals that the width and distribution of gas channel and current collector land area are key optimization parameters for the cell performance improvement.

Keywords: PEM fuel cell; High operating temperature; Local overpotential; Numerical simulation; CFD

1. Introduction

Proton exchange membrane (PEM) fuel cells are electrochemical devices that directly convert the energy from the chemical reaction into electricity. Useful features such as high power density, simple, safe construction and fast start-up make those particularly suitable for home appliance, vehicles and transportation tools [1]. Generally, PEM fuel cells operate at temperature below 363 K, allowing for faster start-up and immediate response to changes in the demand for power [2]. It is well known that the operating temperature has a significant influence on PEM fuel cell performance [3]. The increase in the operating temperature is beneficial to fuel cell performance since it increases reaction rate and higher mass transfer rate but usually lowers cell ohmic resistance arising from the higher ionic conductivity of the electrolyte membrane. In addition, at high temperature, CO poisoning can be alleviated by reducing chemisorptions of CO [4]. A great deal of effort has been expended in the development of new kinds of membranes for PEM fuel cells that perform efficiently at high temperature [5–10]. Recently, much more attention has been paid to high temperature PEM fuel cells-based on the temperature resistant polymer polybenzimidazole (PBI) membrane, which allows to work at temperature up to 473 K [11,12]. Another advantage of PBI-based PEM fuel cell is that such system does not require humidification of the membrane [13]; traditional membrane such as sulfonated fluourocarbon polymer (e.g. Nafion) requires remaining hydrated during the fuel cell reaction. To keep the membrane hydrated, the system generally includes a sub-system that humidifies the cathode air stream to prevent the air stream from drying out the membrane as the air is flowed through the fuel cell. Therefore, development of PBI membrane-based fuel cell operating at high temperature could lead a simple PEM fuel cell. However, problematic aspects such as material problems related to corrosion, electrode degradation, electrocatalyst sintering as well as re-crystallization and electrolyte loss by evaporation are also accelerated at higher operating temperature. These material constraints limit the temperatures at which the various fuel cells can be effectively operated. In order to improve and optimize the PEM fuel cell design, it is extremely important to understand

* Corresponding author. Tel.: +82 31 280 9336; fax: +82 31 280 9359.
E-mail address: sj0514.lee@samsung.com (S.J. Lee).

0378-7753/$ – see front matter © 2006 Elsevier B.V. All rights reserved.
doi:10.1016/j.jpowsour.2006.08.001

the thermal and electrochemical behavior under various design and operating conditions.

The experimentally difficult environment of fuel cell system has motivated development of models that can simulate and predict the performance of PEM fuel cells. Extensive research efforts have been devoted in the past decade. The first one-dimensional models were published in the early 1990s by Springer et al. [14] and Bernardi and Verbrugge [15]. More recently, computational fluid dynamic (CFD) and improved transport models have made the development of more realistic computational model feasible. A number of PEM fuel cell models for the general operating temperature cases have appeared in the literatures [16–22]. However, future studies are still in need, especially for PEM fuel cell operating at high temperature, where water is in the vapor phase and the membrane has a water electro-osmosis drag force near zero. Under this condition, the performance of membrane would be relatively independent of the humidity, and thus the water management becomes easier or even unnecessary [23–25].

In this paper a single-phase, three-dimensional, non-isothermal model for PEM fuel cell at high operating temperature ($T \geq 393$ K) is presented to describe the fundamental processes occurring in each components of a fuel cell—current collector, gas flow channels, gas diffusion layers (GDL), catalyst layers (CL) and the membrane. Two electric potential field equations were solved. One potential field was solved in the membrane and catalyst layers. The other was solved in the catalyst layers, the gas diffusion layers and the current collectors. The Bulter–Volmer equations were used to describe the relationship between the current density and the local overpotential. The convection and diffusion of different species in the gas flow channel and gas diffusion layer were also considered. The temperature effects on mass diffusivity and electric conductivity were taken into account. The heat capacity, gas viscosity and thermal conductivities of each gas were assumed to be polynomial functions of temperature. The model was implemented into the commercial CFD code FLUENT 6.1 with custom developed user-define functions (UDF) [26].

2. Physical and numerical model

Fig. 1 schematically shows a PEM fuel cell divided into the following sub-regions: the current collector, gas flow channel, gas diffusion layer and catalyst layer in the anode and cathode sides and the membrane in the middle. The reactant feed is conveyed by the gas flow channel and distributed onto the anode and cathode. Reactants pass through the respective porous GDLs and reach the CLs where the electrochemical reaction occurs. The membrane acts as the gas separator, electrolyte and the proton conductor. The electrons are collected by the anode current collector, which is connected to cathode current collector through the external load.

2.1. Assumptions

In this model, the anode feed is pure hydrogen and air is paralleled in the cathode gas channel. The fuel cell is assumed to operate in steady state under constant load conditions. Since

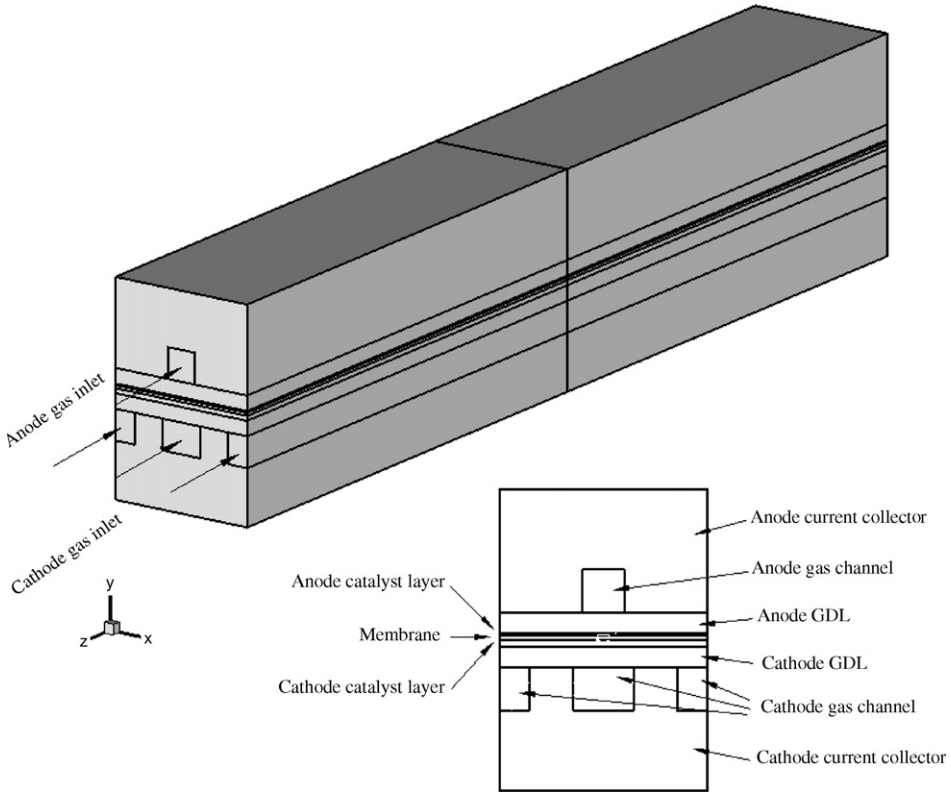

Fig. 1. Schematic model of a PEM fuel cell.

the gas streams in the flow channel are at low velocities (or low Reynolds number), laminar flow and ideal gas behavior are assumed. Additional assumptions are as follows:

(1) All water produced by the electrochemical reaction is assumed to be vaporous phase due to the high operating temperature and water transportation across the membrane is ignored since water drag coefficient for high temperature membrane is low.
(2) Dilute solution theory is used to determine the species diffusion.
(3) The membrane is considered impermeable to gases. The crossover of reactant gases and product water is neglected.
(4) Ohmic heating in the current collector, GDL and CL is neglected because of their high electric conductivity.
(5) Both GDL and CL are assumed to be homogeneous and isotropic.

2.2. Governing equations

A steady state, single-phase, isothermal model of PEM fuel cell consists of five principles of conservation: mass, momentum, species, energy and charge. Thus, the governing equations can be written, in vector form, as

$$\text{Continuity}: \quad \nabla \cdot (\rho \boldsymbol{u}) = S_{\mathrm{m}}, \tag{1}$$

where $\boldsymbol{u}$ denotes the superficial velocity vector in the porous media. ρ is the density of gas mixture, which can be calculated by using

$$\rho = \frac{1}{\sum_k Y_k/\rho_k}, \tag{2}$$

where ρ_k is the density of species k and it can be obtained from the ideal gas law relation

$$\rho_k = \frac{pM_k}{RT}, \tag{3}$$

where p is the gas pressure and M_k is the molecular weight and R is the universal gas constant.

$$\text{Momentum}: \quad \frac{1}{\varepsilon^2}\nabla \cdot (\rho \boldsymbol{u}\boldsymbol{u}) = -\nabla p + \nabla \cdot \boldsymbol{\tau} + S_{\mathrm{u}}, \tag{4}$$

where ε is the porosity of the electrode materials. $\boldsymbol{\tau}$ is the viscous stress tensor.

$$\text{Species}: \quad \nabla \cdot (\rho \boldsymbol{u} Y_k) = \nabla \cdot \boldsymbol{J}_k + S_k, \tag{5}$$

where $\boldsymbol{J}_k$ is the diffusive mass flux vector, which can be written as

$$\boldsymbol{J}_k = -\sum_{j=1}^{N-1} \rho D_{kj} \nabla Y_j. \tag{6}$$

Here D_{kj} is the binary-diffusion coefficient, which depends on temperature and pressure and can be calculated according to the empirical expression [27]

$$D_{kj} = \frac{T^{1.75}(1/M_k + 1/M_j)^{1/2}}{p((\sum_{\mathrm{l}} V_{\mathrm{l}k})^{1/3} + (\sum_{\mathrm{l}} V_{\mathrm{l}j})^{1/3})^2} \times 10^{-3}, \tag{7}$$

where $V_{\mathrm{l}k}$ is the atomic diffusion volume, and the value of $\sum V_{\mathrm{l}k}$ is given by Cussler [27].

$$\text{Energy}: \quad \nabla \cdot (\boldsymbol{u}(\rho E + p)) = \nabla \cdot \left(\lambda_{\mathrm{eff}} \nabla T - \sum_k h_k \boldsymbol{J}_k + (\boldsymbol{\tau}_{\mathrm{eff}} \cdot \boldsymbol{u}) \right) + S_{\mathrm{h}}, \tag{8}$$

where h_k is the enthalpy of species k. $\boldsymbol{\tau}_{\mathrm{eff}}$ is the effective stress tensor, which can be ignored due to the low velocity of laminar gas flow. λ_{eff} is the effective thermal conductivity in a porous material consisting of the electrode solid matrix and gas, which is given by

$$\lambda_{\mathrm{eff}} = \varepsilon \lambda_{\mathrm{f}} + (1 - \varepsilon)\lambda_{\mathrm{s}}, \tag{9}$$

where λ_{s} is the thermal conductivity of the electrode solid matrix and λ_{f} is the thermal conductivity of the gas, which can be expressed as a polynomial function of temperature

$$\lambda_{\mathrm{f}} = A_0 + A_1 T + A_2 T^2 + A_3 T^3, \tag{10}$$

where A_i, $i = 0, \ldots, 3$ can be determined by the experiment of real gases, as seen in Appendix A. Similar to the thermal conductivity, the viscosity and heat capacity of each gas species can also be described by the polynomial expression of temperature with empirical coefficients.

$$\text{Charge}: \quad 0 = \nabla \cdot (\kappa_{\mathrm{sol}} \nabla \phi_{\mathrm{sol}}) + S_{\mathrm{sol}}, \tag{11}$$

$$0 = \nabla \cdot (\kappa_{\mathrm{mem}} \nabla \phi_{\mathrm{mem}}) + S_{\mathrm{mem}}, \tag{12}$$

where solid potential Eq. (11) accounts for the electron transport through the electrode solid conductive materials; the membrane potential Eq. (12) represents the proton transport through the membrane. κ_{sol} and κ_{mem} are electronic conductivity of electrode and ionic conductivity of membrane.

There are six source terms, S_{m}, S_{u}, S_k, S_h, S_{sol} and S_{mem}, which represent various volumetric sources or sinks arising from each sub-region of a fuel cell. Details of the various source terms are summarized in Table 1. It shows that either generation or consumption of gas species k and creation of electric current occurs only in the CL where the electrochemical reactions take place. S_{m}, S_k, S_h, S_{sol} and S_{mem} terms are therefore related to the transfer current through the solid conductive materials and the membrane. The transfer current at anode and cathode can be described by Butler–Volmer equations as follows [28]:

$$j_{\mathrm{a}} = i_{\mathrm{a}}^{\mathrm{ref}} \left(\frac{p_{\mathrm{H_2}}}{p_{\mathrm{H_2}}^0} \right)^{\beta} \left[\exp\left(\frac{\alpha_{\mathrm{a}} F \eta_{\mathrm{a}}}{RT} \right) - \exp\left(-\frac{\alpha_{\mathrm{c}} F \eta_{\mathrm{a}}}{RT} \right) \right], \tag{13}$$

$$j_{\mathrm{c}} = i_{\mathrm{c}}^{\mathrm{ref}} \left(\frac{p_{\mathrm{O_2}}}{p_{\mathrm{O_2}}^0} \right)^{\beta_1} \left(\frac{p_{\mathrm{H_2O}}}{p_{\mathrm{H_2O}}^0} \right)^{\beta_2} \times \left[\exp\left(-\frac{\alpha_{\mathrm{c}} F \eta_{\mathrm{c}}}{RT} \right) - \exp\left(\frac{\alpha_{\mathrm{a}} F \eta_{\mathrm{c}}}{RT} \right) \right], \tag{14}$$

Table 1
Source terms for continuity, momentum, species, energy and charge conservation equations in various regions of a polymer electrolyte fuel cell

	Source terms			
	Flow channels	GDL	GCL	Membrane
Continuity	$S_m = 0$	$S_m = 0$	$S_m = -\frac{M_{H_2}}{2F} j_a$, for anode side $S_m = -\frac{M_{O_2}}{4F} j_c + \frac{M_{H_2O}}{2F} j_c$, for cathode side	–
Momentum	$S_u = 0$	$S_u = -\frac{\mu}{K_{GDL}}$	$S_u = -\frac{\mu}{K_{GCL}}$	–
Species	$S_k = 0$	$S_k = 0$	$S_k = -\frac{M_{H_2}}{2F} j_a$, for H_2 $S_k = -\frac{M_{O_2}}{4F} j_c$, for O_2 $S_k = \frac{M_{H_2O}}{2F} j_c$, for H_2O	
Energy	$S_h = 0$	$S_h = 0$	$S_h = 0$, for anode side $S_h = \frac{\lvert j_c \rvert}{2F} T\lvert\Delta s\rvert + \lvert j_c \eta_c \rvert$, for cathode side	$S_h = \frac{I^2}{\kappa_{mem}}$
Change	$S_{sol} = 0$	$S_{sol} = 0$	$S_{sol} = -j_a$ on anode side $S_{sol} = j_c$ on cathode side	$S_{sol} = 0$
	$S_{mem} = 0$	$S_{mem} = 0$	$S_{mem} = j_a$ on anode side $S_{mem} = -j_c$ on cathode side	$S_{mem} = 0$

where $F = 96{,}487\ \mathrm{C\ mol^{-1}}$ is the Faraday constant. p_{H_2}, p_{O_2} and p_{H_2O} are the partial pressure of the reactant gases. p^0 is the standard pressure. $p^0_{H_2O}$ is the vapor pressure of the steam at the operating temperature, which can be found from steam Tables. α_a and α_c are the anodic and cathodic charge transfer coefficients. i_a^{ref} and i_c^{ref} is the reference exchange current density, which depends on the local temperature,

$$i_a^{ref} = i_{a,0}^{ref} \exp\left[-\frac{E_{A,a}}{R}\left(\frac{1}{T} - \frac{1}{T_0}\right)\right], \tag{15}$$

$$i_c^{ref} = i_{c,0}^{ref} \exp\left[-\frac{E_{A,c}}{R}\left(\frac{1}{T} - \frac{1}{T_0}\right)\right], \tag{16}$$

where $E_{A,c}$ and $E_{A,a}$ is the active energy [29], $i_{a,0}^{ref}$ and $i_{c,0}^{ref}$ is the anodic and cathodic reference exchange current densities at reference temperature T_0, see in Table 2. β, β_1 and β_2 are empirically determined concentration parameters for $\beta = 0.25$, $\beta_1 = 0.5$ and $\beta_2 = 0.25$ [28]. As the partial pressure decreases, the exchange current density also decreases, resulting in a decrease of cell performance. The local overpotential η_a and η_c in Eqs. (13) and (14) can be expressed as [30]

$$\eta_a = \phi_{sol} - \phi_{mem}, \tag{17}$$

$$\eta_c = \phi_{sol} - \phi_{mem} - V_0. \tag{18}$$

Here V_0 is the thermodynamic equilibrium potential, which can be given by ($T > 373.15$ K)

$$V_0 = 1.17 - 2.756 \times 10^{-4}(T - 373.15) + 4.308 \times 10^{-5} \ln\left(\frac{a_{H_2}(a_{O_2})^{1/2}}{a_{H_2O}}\right). \tag{19}$$

This equilibrium potential is calculated from thermodynamic data of reaction enthalpy and entropy changes while the product water is in gaseous phase. The definition of a_{H_2}, a_{O_2} and a_{H_2O} are

$$a_{H_2} = \frac{p_{H_2}}{p^0}, \qquad a_{O_2} = \frac{p_{O_2}}{p^0}, \qquad a_{H_2O} = \frac{p_{H_2O}}{p^0_{H_2O}}. \tag{20}$$

The temperature dependence of the membrane conductivity can be accurately described by the Arrhenius equation [31]

$$\kappa_{mem} = \kappa_0 \exp\left[-\frac{E_{A,\kappa}}{R}\left(\frac{1}{T} - \frac{1}{T_0}\right)\right], \tag{21}$$

where $E_{A,\kappa}$ is the activation energy and κ_0 is the pre-exponential factor.

The heat release from CL of the PEM fuel cell is caused by the changes of enthalpy and irreversibility related to charge

Table 2
Electrochemical and thermal properties

Parameter	Symbol	Value	Unit
Porosity of GDL	ε	0.8	–
Porosity of GCL	ε	0.6	–
GDL/GCL hydraulic permeability		1.0e−15	–
Membrane ionic conductivity	κ_0	12.99	$\mathrm{S\ m^{-1}}$
GDL/GCL electric conductivity	κ	103.3	$\mathrm{S\ m^{-1}}$
Electrode electric conductivity	κ	535	$\mathrm{S\ m^{-1}}$
Anodic charge transfer coefficient	α_a	1.0	–
Cathodic charge transfer coefficient	α_c	1.0	–
Anode reference exchange current density	$i_{a,0}^{ref}$	1.0e8	$\mathrm{A\ m^{-3}}$
Cathode reference exchange current density	$i_{c,0}^{ref}$	1.7e2	$\mathrm{A\ m^{-3}}$
Thermal conductivity of GCL		1.7	$\mathrm{W\ m^{-1}\ k^{-1}}$
Thermal conductivity of membrane		0.95	$\mathrm{W\ m^{-1}\ k^{-1}}$
Thermal conductivity of GDL		1.7	$\mathrm{W\ m^{-1}\ k^{-1}}$
Thermal conductivity of current collector		25	$\mathrm{W\ m^{-1}\ k^{-1}}$

transfer [21]. According to the assumption, the ohmic heating is ignored in the current collector, GDL and CL but considered in the membrane due to the relative low ionic conductivity of membrane. Empirically, the change of entropy Δs, as a function of temperature T, can be expressed as [2]

$$\Delta s = 33.64 + 4.52564 \times 10^{-2} T - 2.98397 \times 10^{-5} T^2 + 3.40625 \times 10^{-9} T^3 - 2.60417 \times 10^{-12} T^4. \quad (22)$$

This equation is a good approximate for temperature from 373 K to 1137 K.

Once membrane potential, ϕ_{mem} and membrane conductivity, κ_{mem} are obtained, local current density, $\boldsymbol{I}$, can be calculated by

$$\boldsymbol{I} = -\kappa_{mem} \nabla \phi_{mem}. \quad (23)$$

The average current density, which is the average of the local current density over the entire membrane, can be obtained by

$$I_{avg} = \frac{1}{A_{mem}} \int_{A_{mem}} \boldsymbol{I} \cdot d\boldsymbol{A}, \quad (24)$$

where A_{mem} is the membrane area.

2.3. Boundary conditions

On the inlet boundaries of anode and cathode flow channels, the stoichiometric mass flow rate and mass fractions of species were prescribed with the gas temperature equal to the operating temperature, as seen in Table 3. The pressure boundary conditions were used at the outlet. As there is no protonic current leaving the fuel cell through any external boundary, zero flux boundary condition for ϕ_{mem} was applied on all outside boundaries. However, there are external boundaries on the anode and cathode side, which contact with the external electric circuit and the electrical current is generated only through these boundaries. Therefore, a prescribed fixed value for ϕ_{sol} was used on these boundaries. The anode side was set to zero and the value prescribed on the cathode side is the cell operating voltage. Zero flux boundary condition for ϕ_{sol} was applied on remaining external boundaries. As the reactant gases are dielectric, zero flux of ϕ_{sol} and ϕ_{mem} are enforced at the interface between the electrode and the flow channel.

Table 3
Geometrical and operating parameters

Parameter	Value	Unit
Cell width	3.4	mm
Channel length	235	mm
Channel height	0.7	mm
Anode channel width	0.7	mm
Cathode channel width	1.0	mm
Anode GDL thickness	0.34	mm
Anode GCL thickness	0.04	mm
Membrane thickness	0.065	mm
Cathode GCL thickness	0.11	mm
Cathode GDL thickness	0.34	mm
Electrode height	2.0	mm
Operating temperature	398–433	K
Anode stoichiometric mass flow rate	1.5	–
Cathode stoichiometric mass flow rate	2.0	–
Anode outlet pressure	1.1	atm
Cathode outlet pressure	1.1	atm
Anode inlet mass fraction H_2	1.0	–
Cathode inlet mass fraction O_2:N_2	0.22:0.78	–

Due to the structure of the FLUENT CFD code, the interface between the membrane and CL is defined as a wall in order to prevent any crossover of species through the membrane. The wall has a fluid region on each side. This was implemented by creating a "shadow" of the wall cell layer by the FLUENT automatically. According to the physical property of electrolyte membrane, only protons are allowed to transfer though the electrolyte membrane. Therefore, zero flux of ϕ_{sol} is defined at this internal wall. However, for the ϕ_{mem}, the continuous flux boundary conditions should be applied and it can be expressed as

$$(\kappa_{mem} \nabla \phi_{mem}) \cdot \boldsymbol{n}^-|_- = (\kappa_{mem} \nabla \phi_{mem}) \cdot \boldsymbol{n} + |_+, \quad (25)$$

where symbol '−' and '+' stand for two sides of the internal wall. $\boldsymbol{n}$ denotes the exterior normal vector of the internal wall. The flux continuous boundary conditions were enforced by the custom developed UDF.

On the interface between GDL and catalyst layer, zero flux of ϕ_{mem} is defined because protons transfer mainly through the electrolyte materials. However, since the current collector is electric, the flux of ϕ_{sol} across the areas should be continuous. The UDF is implemented to enforce the continuous flux of ϕ_{sol} and it can be expressed as

$$(\kappa_{sol} \nabla \phi_{sol}) \cdot \boldsymbol{n}^-|_- = (\kappa_{sol} \nabla \phi_{sol}) \cdot \boldsymbol{n}^+|_+. \quad (26)$$

As shown in Fig. 1, the fuel cell with single straight gas channel was employed, and the fuel cell flow plate was formed with a plurality of gas channels. Therefore, the symmetrical boundary condition is applied on the side walls normal to x-axis and no-slip boundary condition is applied on remaining walls for the momentum equations.

The model was implemented via a set of user-defined functions in a commercial CFD code, FLUENT 6.1, which is a parallel code using the finite volume method and iterative segregated implicit solver. Second order discretization schemes were

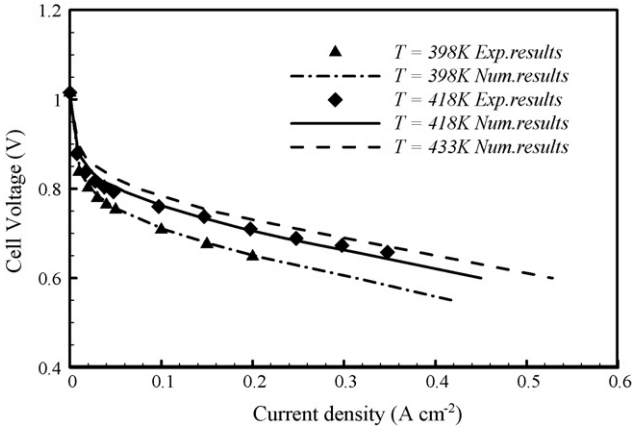

Fig. 2. Polarization curve: comparison of simulations and experiments.

used for all transport equations. More details of the numerical procedure can be found from the literature of former researchers [32,33]. Stringent numerical tests were performed to ensure that the solutions are independent of the grid size. A mesh with about 180,000 grid points was found to provide sufficient spatial resolution. The solution was considered to be convergent when the relative error in each field between two consecutive iterations was less than 10^{-6}.

3. Results and discussion

Fig. 2 shows the comparison of polarization curves obtained from numerical prediction and experimental results at different operating temperatures. In both cases, the cell was operated at constant temperature and without any humidification, i.e. with dry gases. It can be seen that the model predicts results close to the experimental data. In Eq. (19), it can be seen that

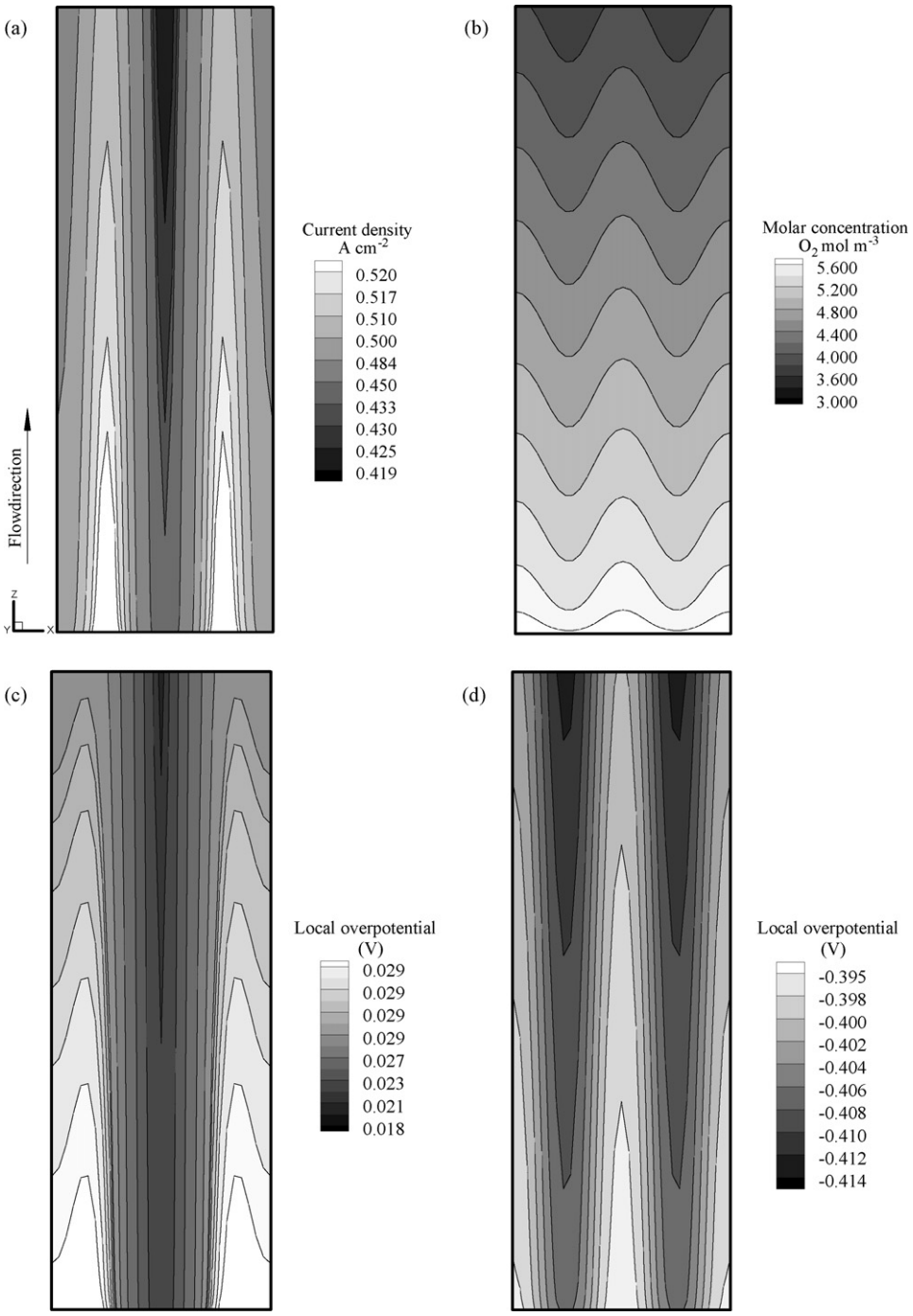

Fig. 3. Distributions for current density, concentration of oxygen and local overpotential at $V_{cell} = 0.6$ V, $I_{avg} = 0.485$ A cm^{-2} and $T = 433$ K: (a) average current density distribution at the membrane; (b) oxygen molar concentration distribution at the cathode CL; (c) local overpotential η_a distribution at anode CL; (d) local overpotential η_c distribution at cathode CL.

the thermodynamic equilibrium potential decreases as operating temperature increases. However, with the increasing current density, the cell voltage is mainly dominated by the ohmic loss. Membrane ionic conductivity increases with the increasing of operating temperature (Eq. (21)). Therefore, at the high operating temperature, ohmic loss decreases and the cell performance is improved.

3.1. Isothermal model

Fig. 3 shows the average current density, concentration and local overpotential distribution for $V_{cell} = 0.6$ V, $I_{avg} = 0.485$ A cm^{-2} obtained using the isothermal model. Since the electric current path from the areas of CL under the gas channel is longer than the path from the area of CL under the current collector land areas, the current density maxima locate under the current collector land area because of the influence of the ohmic losses in the CL and GDL (in Fig. 3(a)). The concentration of oxygen under the current collector is smaller than concentration under the gas channel due to consumption (in Fig. 3(b)). The concentration of oxygen in the cathode CL decreases monotonically along with the gas flow direction as the electrochemical reaction proceeds. Therefore, the current density also decreases along with the flow direction.

Fig. 3(c) and (d) show the local overpotential (η_a and η_c) distribution on the CL. η_a decreases along with the flow direction and maxima locate under the current collector land area. This is coincident with the distribution of current density. However, for the local overpotential η_c at the cathode CL, the absolute value increases along with the flow direction (seen in Fig. 3(d)). This results from the ohmic loss along with the flow direction decreased by the decrease in current density. The results are different from those in [21], where only the overpotential at the cathode is considered and the anodic overpotential is assumed to be constant. Fig. 4 shows the distribution of solid potential ϕ_{sol} at the solid electrode. Because of the lateral electronic resistance, the minima solid potential locates at the anode CL under the gas flow channel, while the maxima appears at the cathode CL under the gas flow channel, resulting in the relative slower electrochemical reactions and hence lower current density. The *iso*-potential lines are normal to the flow channel and side walls since the fuel gas is assumed to be insulated and the symmetrical boundary conditions are applied on the side walls. The distribution exhibits gradient in both x and y direction due to the non-uniform local current production in the CL and shows that ohmic losses are larger in the CL under gas channels. Fig. 5 shows the distribution of membrane potential ϕ_{mem} at the membrane. As indicated, due to non-uniform local current production in the adjacent CL, the gradients in both x and y direction also exist. The membrane potential along with the anode side interface is not uniform, which is absolutely different from that assumption in [21].

The effect of the width of gas channel on cell performance is shown in Fig. 6 where the width of both anode and cathode gas channels are set to be 0.7 mm and 1.0 mm. The average current densities are $I_{avg,0.7} = 0.526$ A cm^{-2} and $I_{avg,1.0} = 0.474$ A cm^{-2} with operating voltage $V_{cell} = 0.6$ V. The average current density

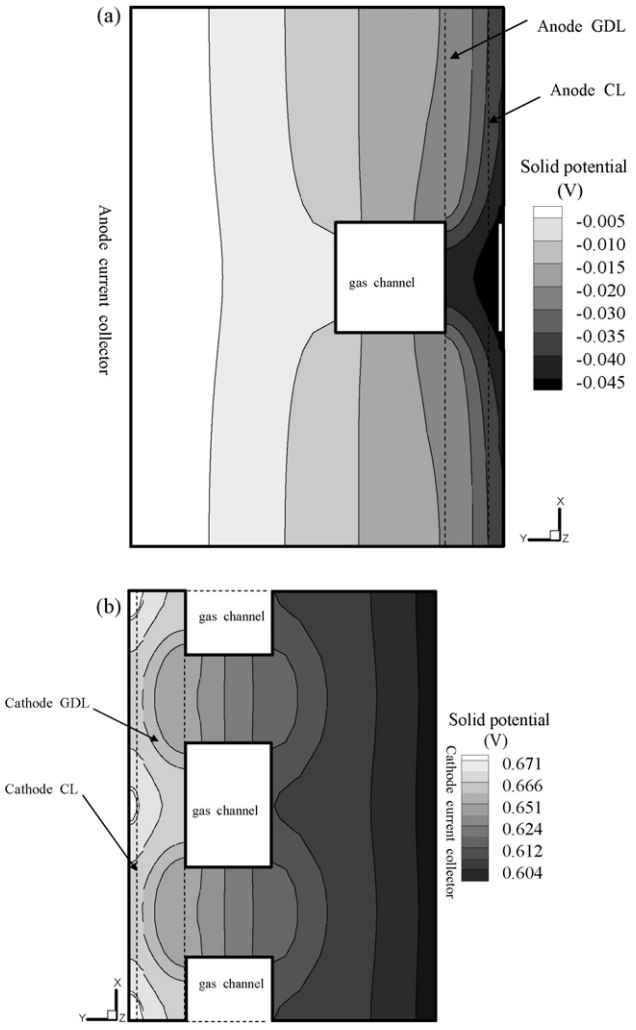

Fig. 4. Solid potential distribution in the current collector, GDL and CL on the (a) anode and (b) cathode side at $V_{cell} = 0.6$ V, $T = 433$ K.

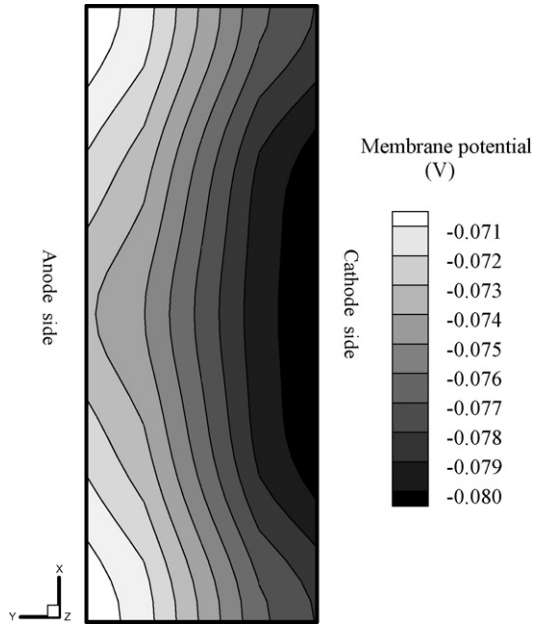

Fig. 5. Membrane potential distribution in fuel cell membrane at $V_{cell} = 0.6$ V, $T = 433$ K.

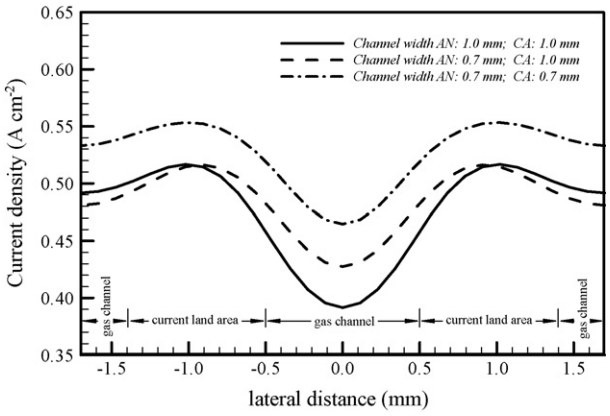

Fig. 6. Current density distribution in the lateral direction in the middle of the cell with different channel width at $V_{cell} = 0.6$ V, $T = 433$ K.

is increased with the decreasing of gas channel. The current collector land area is enlarged while the width of gas channel is decreased. The ohmic losses are decreased due to the fact that electric current path from CL to the current collector land area is shortened. Therefore, the average current density is increased at the operating point where the cell voltage is essentially dominated by ohmic loss. On the other hand, it is predictable that with decreasing of gas channel width, the average current density will be decreased in the operating point where the cell voltage is essentially dominated by mass transport of fuel gas. From Fig. 6, it can be seen that the maxima values of current density locate under the current collector land. Close to the margin region, though current collector land area with anode gas channel width 1.0 mm is smaller than that with anode gas channel width 0.7 mm, the former current density is larger than the latter, because more hydrogen gas can be supplied with increasing of anode gas channel width.

It is well known that the fuel cell itself has many trade-off options. The pressure loss along the gas channel is increased with the increasing of gas channel width and the operating parasitic power consumption is increased. Therefore, it is critical to optimize the width and distribution of gas channel and current collector land area in order to improve cell performance after the cell operating point is determined.

3.2. Non-isothermal model

As we have presented, the heat is released from CL of the PEM fuel cell through the electrochemical reaction and from the membrane by ohmic resistance. Fig. 7 shows the temperature distribution of the membrane with the inlet gas temperature $T = 433$ K. For low current density state, (Fig. 7(a)), the temperature difference from the inlet gas temperature is small and the temperature maxima locate under the gas channel. This is caused by the difference of thermal conductivity between reactant gases and the electrode. As the temperature is increased with the increase in current density, the temperature maxima appear near the outlet boundary (Fig. 7(b)). Fig. 8 shows the temperature distribution on the midway section of the fuel cell. The *iso*-temperature lines are normal to the side boundary because symmetrical boundary conditions were applied. In low current density (Fig. 8(a)), the maxima of temperature locate in the

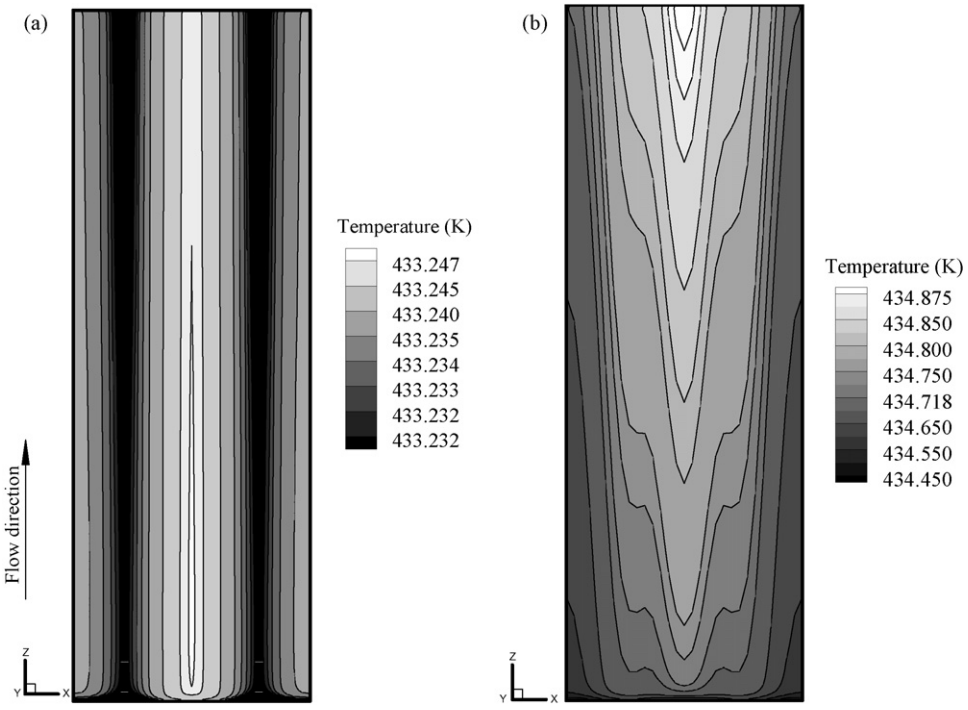

Fig. 7. Temperature distribution contour on the membrane: (a) low current density $I_{avg} = 0.075$ A cm^{-2}, $V_{cell} = 0.8$ V; (b) high current density $I_{avg} = 1.025$ A cm^{-2}, $V_{cell} = 0.4$ V.

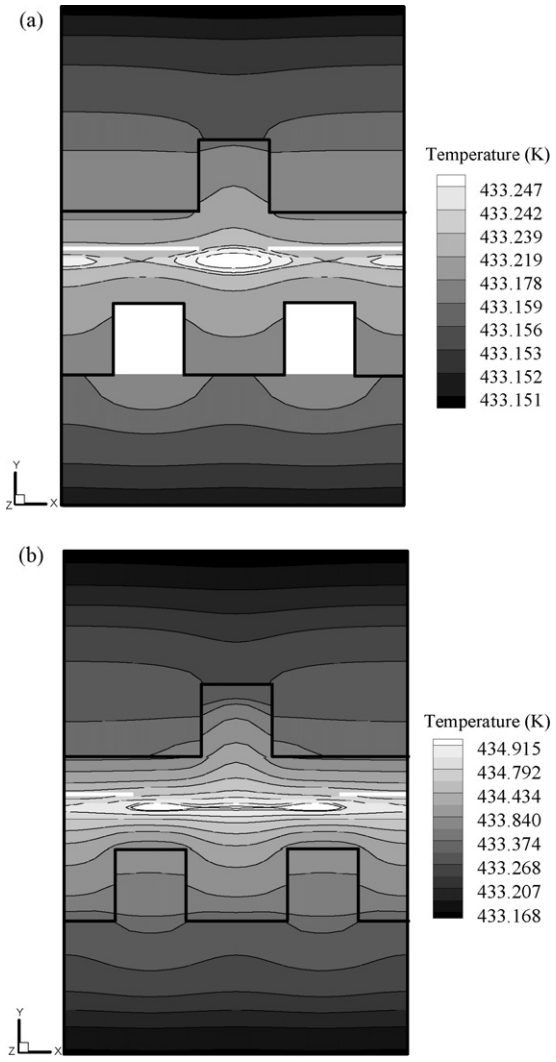

Fig. 8. Temperature distribution on midway section of the fuel cell: (a) low current density $I_{avg} = 0.075\ A\ cm^{-2}$, $V_{cell} = 0.8\ V$; (b) high current density $I_{avg} = 1.025\ A\ cm^{-2}$, $V_{cell} = 0.4\ V$.

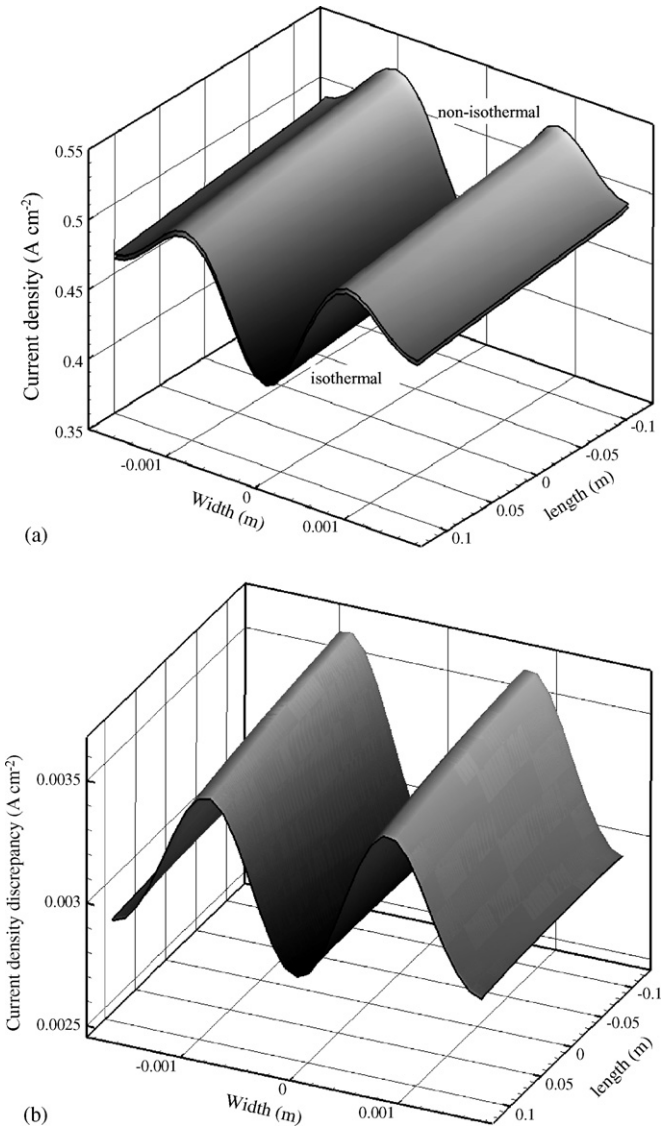

Fig. 9. The effect of temperature on current density distribution while $V_{cell} = 0.6\ V$: (a) current density distribution with isothermal and non-isothermal state; (b) relative difference between the computed current density profiles of isothermal and non-isothermal state.

cathode CL under the gas channel. However, in high current density (Fig. 8(b)), it is observed that the maxima of temperature shift to the position under the current collector land area. This can be explained by the increased ohmic heat in the membrane at high current density state. The temperature variation is also increased with the increasing of current density. The influence of thermal results on the performance of fuel cell is shown in Fig. 9, where the profiles of current density across the membrane are presented. From Fig. 9(a), the current density is increased when the heat exchange is considered, since the temperature inside the fuel cell is larger than the temperature at the surface that can always be recognized as the operating temperature. The difference between these two results can be seen in Fig. 9(b), where the maxima of difference appear under the collector land areas. Therefore, both the current density distribution and temperature distribution are closely related with the geometry structure and dimension of the current collector land area.

4. Conclusion

In this paper, a three-dimensional, single-phase, non-isothermal PEM fuel cell model at high operating temperature ($T \geq 393\ K$) was developed and implemented in the framework of a CFD code. Water was considered to be in vaporous phase and the water transportation across the membrane was ignored because of its low water electro-osmosis drag force. The complete set of conservation equations of mass, momentum, energy, species and charge were numerically solved with proper account of electrochemical kinetics. The electron transport equation was solved in the CL, GDL and current collectors rather than assumed uniform and constant, rendering more accurate prediction of local overpotential and current density.

A single straight-channel PEM fuel cell at operating temperature $T = 433\ K$ was numerically studied in detail with focus on

Table A.1
Coefficients of polynomial expression of gas properties

Item	A_0	A_1	A_2	A_3
Thermal conductivity				
H_2	4.3484×10^{-2}	4.8712×10^{-4}	-1.4917×10^{-7}	4.6636×10^{-11}
H_2O	5.1348×10^{-3}	1.8280×10^{-6}	1.5895×10^{-7}	-7.8887×10^{-11}
N_2	6.9408×10^{-4}	9.7432×10^{-5}	-5.0467×10^{-8}	1.5163×10^{-11}
O_2	5.5780×10^{-4}	9.5339×10^{-5}	-3.1382×10^{-8}	7.1220×10^{-12}
CO_2	-8.5816×10^{-3}	8.5843×10^{-5}	-1.4887×10^{-9}	-7.9582×10^{-12}
Viscosity				
H_2	2.6488×10^{-6}	2.2381×10^{-8}	-5.0735×10^{-12}	8.2349×10^{-16}
H_2O	-3.1387×10^{-6}	4.1514×10^{-8}	0	0
N_2	3.3349×10^{-6}	5.4210×10^{-8}	-2.1159×10^{-11}	4.1614×10^{-15}
O_2	2.8879×10^{-6}	6.6299×10^{-8}	-2.5463×10^{-11}	4.9740×10^{-15}
CO_2	7.5190×10^{-8}	5.5156×10^{-8}	-1.8831×10^{-11}	3.4136×10^{-15}
Heat capacity				
H_2	1.3550×10^{-4}	3.6304	-4.6474×10^{-3}	2.2471×10^{-6}
H_2O	2.0963×10^{-3}	-9.1474×10^{-1}	1.6648×10^{-3}	-5.5865×10^{-7}
N_2	1.0732×10^{-3}	-2.6917×10^{-1}	5.9522×10^{-4}	-2.3165×10^{-7}
O_2	8.3669×10^{-2}	2.5830×10^{-1}	7.7057×10^{-5}	-8.0416×10^{-8}
CO_2	5.0437×10^{-2}	1.4174	-9.0900×10^{-4}	2.2287×10^{-7}

the temperature distribution and cell performance. Overall, the model was in a good agreement with experimental results. The current density increases with the increasing of operating temperature, demonstrating a necessity for non-isothermal modeling of PEM fuel cells. The maxima current density occurs under the current collector land areas as a result of the dominant influence of ohmic losses over concentration losses. It shows that the width and distribution of gas channel and current collector land are key optimization parameters for better cell performance. The temperature maxima locate in the cathode CL and the temperature variation across the fuel cell increases with the increasing of current density.

Appendix A

According to the experiment of real gases, the thermal conductivity, viscosity and heat capacity of each gas species can be described by polynomial expression of temperature

$$\lambda_f = A_0 + A_1 T + A_2 T^2 + A_3 T^3, \quad \text{(A.1)}$$

where the value of A_i, $i = 0, \ldots, 3$ can be found in the following Table A.1.

References

[1] S. Srinivasan, R. Mosdale, P. Stevens, C. Yang, Rev. Energy Environ. 24 (1999) 281.
[2] J. Larminie, A. Dicks, Fuel Cell Systems Explained, John Wiley and Sons Ltd., New York, USA, 2000.
[3] C. Yang, P. Costamagna, S. Srinivasan, J. Benziger, A.B. Bocarsly, J. Power Sources 103 (2001) 1.
[4] Q.F. Li, R.H. He, J.O. Jensen, N.J. Bjerrum, J. Electrochem. Soc. 150 (12) (2003) A1599.
[5] I. Honma, H. Nakajima, S. Nomura, Solid State Ionics 154–155 (2002) 707.
[6] P. Costamagna, C. Yang, A.B. Bocarsly, S. Srinivasan, Electrochim. Acta 47 (7) (2002) 1023.
[7] Q.F. Li, R.H. He, J.O. Jensen, N.J. Bjerrum, Chem. Mater. 15 (2003) 4896.
[8] S.H. Kwak, T.H. Yang, C.S. Kim, K.H. Yoon, Solid State Ionics 160 (3) (2003) 309.
[9] H.J. Nikhil, D. Katherine, D. Ravindra, Electrochim. Acta 51 (2005) 553.
[10] Y. Song, J.M. Fenton, H.R. Kunz, L.J. Bonville, M.V. Williams, J. Electrochem. Soc. 152 (3) (2005) A539.
[11] Q.F. Li, H.A. Hjuler, N.J. Bjerrum, J. Appl. Electrochem. 31 (7) (2001) 773.
[12] J.A. Asensio, S. Borros, P.G. Romero, J. Electrochem. Soc. 151 (2004) A304.
[13] Q.F. Li, R.H. He, J.O. Jensen, N.J. Bjerrum, Fuel Cells 4 (3) (2004) 147.
[14] T.E. Springer, T.A. Zawodinski, S. Gottesfeld, J. Electrochem. Soc. 136 (1991) 2334.
[15] D.M. Bernardi, M.W. Verbrugge, AIChE J. 37 (1991) 1151.
[16] D. Singh, D.M. Lu, N. Djilali, Int. J. Eng. Sci. 37 (4) (1999) 431.
[17] S. Um, C.Y. Wang, C.S. Chen, J. Electrochem. Soc. 147 (12) (2000) 4485.
[18] T. Zhou, H. Liu, Int. J. Transport Phenom. 3 (2001) 177.
[19] T. Berning, D.M. Lu, N. Djilali, J. Power Sources 106 (2002) 284.
[20] P.T. Nguyen, T. Berning, N. Djilali, J. Power Sources 130 (1-2) (2004) 149.
[21] B.R. Sivertsen, N. Djilali, J. Power Sources 141 (2005) 65.
[22] Y. Wang, C.Y. Wang, J. Electrochem. Soc. 152 (2) (2005) A445.
[23] S.R. Samms, S. Wasmus, R.F. Savinell, J. Electrochem. Soc. 143 (4) (1996) 1225.
[24] D. Weng, J.S. Wainright, U. Landau, R.F. Savinell, J. Electrochem. Soc. 143 (4) (1996) 1260.
[25] O. Sacadogo, B. Xing, J. New Mater. Electrochem. Syst. 3 (2000) 345.
[26] Fluent Incorporated, Fluent 6.0 and 6.1 User's Guide, 2001.
[27] E.L. Cussler, Diffusion Mass Transfer in Fluid Systems, second ed., Cambridge University Press, New York, USA, 1997.
[28] J.D.J. VanderSteen, B. Kenney, J.G. Pharoah, K. Karan, Proceedings of the Canadian Hydrogen and Fuel Cells Conference, September, 2004.
[29] H. Ju, H. Meng, C.Y. Wang, Int. J. Heat Mass Trans. 48 (2005) 1303.
[30] H. Meng, C.Y. Wang, J. Electrochem. Soc. 151 (3) (2004) A358.
[31] Y.L. Ma, J.S. Wainright, M.H. Litt, R.F. Savinell, J. Electrochem. Soc. 151 (2004) 8.
[32] H. Meng, C.Y. Wang, Chem. Eng. Sci. 59 (2004) 3331.
[33] J.J. Hwang, C.K. Chen, R.F. Savinell, C.C. Liu, J. Wainright, J. Appl. Electrochem. 34 (2004) 217.